Aluminum-Catalyzed Lateral Growth of Spherulite-Like GeS Thin Films on Insulating Substrates using Vapor Transport: Implications for Electro-Optic Applications

*Qinqiang Zhang†, Ryo Matsumura†, and *Naoki Fukata†‡

† Research Center for Materials Nanoarchitectonics (MANA), National Institute for Materials Science (NIMS), Tsukuba, Ibaraki 305-0044, Japan

‡ Graduate School of Pure and Applied Sciences, University of Tsukuba, Tsukuba, Ibaraki 305-8573, Japan

ABSTRACT

Due to the presence of lone-pair electrons, it is challenging to attain lateral growth of thin films of Group IV monochalcogenides. In this study, lateral growth of germanium monosulfide (GeS) thin films with a minimum thickness of about 20 nm was attained on SiO_2/Si and quartz substrates at a growth temperature of 420 ˚C, employing a combined method that uses an aluminum (Al) catalyst and a pre-deposited amorphous GeS layer. Grown GeS thin films using a 20 nm-thick Al show dendrite structures, likely attributable to defects introduced in the Al layer when deposited at room temperature. Dendrite structures virtually eliminated by annealing substrates at 120 ˚C during Al deposition or by using a 5 nm-thick Al layer deposited at room temperature. Time-dependent changes in grown GeS thin films using a 5 nm-thick Al on SiO_2/Si and quartz substrates were shown to exhibit a lateral growth rate of 2 - 3 μm/sec. The

birefringent properties of grown GeS with a Maltese extinction cross pattern were confirmed using cross-polarized optical microscopy, indicating the formation of a spherulite-like structure. It appears that Mullins-Sekerka instability dominates the growth front at the periphery of circular domains, causing a dendrite morphology. A transition region dominated by kinetic-limited diffusion occurs, forming the spherulite-like structure of GeS. X-ray diffraction and atomic force probe investigation reveal the grown spherulite-like GeS, on insulating substrates, to consist of a layered structure with a flat surface. The single-crystalline area of GeS appears to be larger than 200 nm in size as evaluated by selected area electron diffraction via transmission electron microscopy. This study reveals a potential method of achieving lateral growth of GeS on insulating substrates. This method may facilitate the use of GeS as functional semiconductors for developing next-generation field-effect transistors with potential for all-optical manipulation, such as in-memory sensing and computing devices.

KEYWORDS Lateral growth, germanium monosulfide, Al-catalyzed growth, birefringence, spherulite-like structure

1. INTRODUCTION

Recently-rediscovered Group IV monochalcogenides, such as germanium monosulfide (GeS), are promising layered semiconductors [1–3] ; they exhibit unique properties that include non-toxicity, earth-abundancy [4], a moderate bandgap [5], high Curie temperature [6], Eshelby twist [7], in-plane ferroelectricity [8], photostrictive properties [9] and other useful properties [10–14]. Tin monosulfide (SnS), which has a structure that is analogous to that of GeS, has been shown elsewhere to exhibit bulk photovoltaic properties [15], in-plane ferroelectric domain transitions [16], high carrier mobility [17] and other characteristics of interest [18, 19]. Lateral growth techniques for creating large-area thin films of Group IV monochalcogenides remain a challenge, likely due to the presence of lone-pair electrons, resulting in a higher charge energy between van der Waal layers than that of other transition metal chalcogenides [20]. In our previous investigations, a pre-deposited amorphous technique for taking Mullins-Sekerka instability into account has been studied to achieve lateral growth of GeS thin films [21–23].

Centimeter-scale GeS continuous film has been achieved; however, the observed minimum thickness of the grown GeS is still approximately 100 nm, and bulk-like GeS prisms are generally observed in the center of grown circular GeS domains. Growing GeS thin films laterally is still an ongoing project [24–26].

An effective method of achieving a self-limited growth mechanism or of minimizing thickness in the growth of other two-dimensional materials, such as graphene [27, 28] and transition metal chalcogenides [29–31], is to employ a metal catalyst. The first attempt to apply an appropriate metal catalyst to grow GeS took into account the vapor pressure and eutectic temperature of aluminum (Al) and germanium [32, 33]. The eutectic temperature of both is about 400 ˚C, and it is close to the growth temperature in our previous investigation that employed the pre-deposited amorphous GeS method [34]. Aluminum is a commonly-used metal in the semiconductor industry. It is capable of being formed on the target substrate by thermal deposition and atomic layer deposition [35, 36]. Relaxation methods (e.g., post-annealing) for reducing defects in Al layer when deposited under vacuum conditions, such as atomic voids, internal stresses and so forth, are also applied [37–39]. To attain GeS thin films on insulators, Al as the metal catalyst can be used to provide the appropriate activation energy that will minimize the formation of bulk-like GeS prims [29] and to obtain centimeter-scale crystalline GeS thin films. We believe this study to be the first investigation to use Al as a catalyst for the lateral growth of centimeter-scale continuous GeS thin films. In addition, a slight modification of the susceptor with a tilt angle is also implemented, analogous to the other investigation [40], since the boundary layer [41, 42] that results from fluid dynamics on the target substrates using vapor transport method is considered as an important factor to minimize thickness variation in the pre-deposited amorphous GeS layer and the grown GeS thin films [34, 41, 42].

Based on the aforementioned information, an Al layer as the catalyst, designed to be synergistic with the pre-deposited amorphous GeS layer method, was applied to grow GeS thin films on insulating substrates (SiO_2/Si and quartz). Two substrates, i.e., SiO_2/Si measuring 13 mm × 13 mm and quartz measuring 15 mm × 15 mm were both placed in a region which had a growth temperature of 420 ˚C. The birefringent properties of the grown GeS thin films were observed on both the substrates using an optical microscope with crossed polarizers. The spherulite-like structure of the GeS thin films was confirmed by observation of the Maltese

extinction cross pattern [43, 44]. Spherulite crystals are found in a large number of materials documented elsewhere, including polymers [45], salts [46, 47], metals [48, 49], and several human diseases such as Alzheimer's disease and kidney stones [50, 51]. A growth mechanism for spherulite-like GeS thin films is considered and discussed later in detail in comparison with other investigations [52, 53]. The presence of the spherulite-like structure of GeS thin films is likely attributable to ultrahigh supersaturation-induced condensation at the growth front, resulting in the lateral growth of spherulite-like GeS thin films. The lateral growth rate for nonlinear spherulitic growth obtained here is analogous to the supercooling-like method [54, 55] and is in the order of several micrometers per second (2 - 3 μm/sec). In addition to the observed birefringent properties, grown GeS thin films were investigated in this study by Raman spectroscopy, X-ray diffraction (XRD), scanning electron microscopy (SEM) with energy-dispersive X-ray detection (EDX), transmission electron microscopy (TEM), and atomic force probe. Despite techniques for growing spherulites being more an art than a science [51], emerging cylindrical symmetric rotating crystals [56], and the potential to grow single-crystalline functional materials on insulating substrates, as previously investigated for GeO_2 [57], suggest that grown spherulite-like GeS thin films hold the potential to achieve single-crystalline semiconductors on insulating substrates such as SiO_2/Si and quartz, taking advantage of the substrate engineering synergy that benefits from the kink-pair nucleation mechanism (i.e., the Peierls energy barrier) [58, 59] and paving the way for the development of next-generation GeS field-effect transistors (FETs) with the potential advantage of use in programmable FETs using the optic control method [60–62].

2. RESULTS AND DISCUSSION

Al as the catalyst layer was deposited on SiO_2/Si and quartz substrates using a thermal evaporation apparatus in a range of thicknesses from 5 - 20 nm, deposited at room and elevated temperatures, followed by the vapor transport process for growth of GeS. A horizontal quartz tube with two independently-controlled heating regions was then utilized to proceed with the pre-deposited amorphous GeS layer and the growth of crystalline GeS thin films at elevated temperatures. GeS powder was placed in the upstream heating region of the tube, while substrates (300 nm-SiO_2/Si and quartz) were positioned in the downstream heating region. The

experimental heating profile is analogous to that used in our previous investigations [34]; in addition, a further optimized strategy for locating the susceptor, analogous to other investigations, [40–42] and a fixed growth temperature of 420 ˚C were utilized in the current study. (See details in the Materials and Experimental Methods.) This was simply to minimize, as much as possible, the variation in thickness of the grown GeS thin films on SiO_2/Si and quartz substrates to a greater extent than in our previous studies, in which the thickness of the grown crystalline GeS films varied from 1 μm to 100 nm on a single substrate [34].

In this, the first attempt to apply Al as the catalyst layer for growing GeS thin films, a 20 nm-thick Al layer for 15-min growth of GeS thin films was employed, as shown in Figure 1. The growth of bulk-like GeS prisms and clusters were significantly suppressed as a result of use of the Al catalyst, compared to that without employing Al catalyst, as shown in Supporting Figure S1a-S1c. However, large numbers of dendrite structures were observed in the grown GeS films, as shown in Figure 1a. Two types of dendrite structures were identified here. Type 1 dendrite structures, which are dark in color, occupy a smaller area, whereas Type 2 dendrite structure are pale in color and occupy a larger area. Type 1 dendrite structures are present at the center of the Type 2 dendrite structures. Corresponding EDX mappings of dendrite structures are shown in Figure 1b-f. Lower signal intensities for Ge and S and higher intensities for Si and O are observed in accordance with the smaller dark areas present at the center of Type 2 dendrite structures, indicating that the Type 1 dendrite structure is attributable to the loss of Ge and S (Figures 1b,1c,1e,1f). Analogously, dendrite structures with lower signal intensities for Al are observed in accordance with the large pale areas of dendrite structures as shown in Figures 1a and 1d. The Type 2 dendrite structure is therefore attributable to the loss of Al catalyst. Position-dependent measurements of Raman spectra are shown in Figure 1g from the center (#1 spot) to the edge (#3 spot) of the dendrite structure. All three spots show typical Raman phonon modes for GeS [63] as indicated by B_{3g} at 211 cm^{-1}, A_g at 239 cm^{-1} and Ag at 269 cm^{-1}, respectively representing the vibration mode of the zigzag edge direction, the layer breathing mode and the vibration mode of the armchair edge direction. A stronger peak intensity for the Si substrate at a Raman signal of 521 cm^{-1} is observed at the center of the dendrite structure, due to the loss of grown GeS in Type 1 dendrite structures. The Raman signal of Si is lower at the #2 and #3 spots, likely attributable to the effect of Al. The typical surface morphology of the dendrite structures was evaluated by AFM as shown in Figure 1i. The dendrite structures (darker areas) are thinner,

as shown in the AFM mapping of Figure 1h. The corresponding line profile exhibits two steps in its thickness, from Type 1 to Type 2 dendrite structures. The presence of a lower step (with a Type 1 dendrite structure) and a higher step (with a Type 2 dendrite structure) is therefore attributable to grown GeS and the loss of Al (approximately 20 nm thick), respectively, in the light of the preceding investigations. Grown GeS thin films located at areas without dendrite structures, i.e., at the #3 spot, show a flat surface on SiO_2/Si substrates (Figures 1a and 1h). It thus appears that the dendrite structures are attributable to defects such as internal stress and atomic voids that were already present in the thicker thermally-deposited Al [39, 64]. These defects are aggravated by the elevated temperature of the argon carrier gas containing GeS. Identification of the starting point of dendrite structures will require a great deal of investigation, since it is likely related to the elevated temperature, conditional pressure, speed of argon carrier gas flux, concentration of GeS and other variables. Synergy with simulation methods in fluid dynamics and phase-field models will therefore be examined in future investigations.

The XRD results confirm the orthorhombic structure of GeS to be in accordance with the standard GeS reference (PDF#00-009-0231) as shown in Figure 1i. In the 2θ scan mode, diffraction peaks at 16.9˚ and 34.2˚ are obtained, representing (002) and (004) respectively, indicating that the crystal orientation is along the c-axis (001), and normal to the van der Waals stacking layers. However, additional (102), (012), (110) and (103) peaks are obtained. These can likely be ascribed to the loss of Al, resulting in the formation of other crystal orientations. Representative photographs and optical microphotographs are shown in Figure 1j-l, which reveal almost complete coverage of grown GeS thin film on a 13 mm × 13 mm SiO_2/Si substrate for a growth time of 15 min. The grown GeS film exhibits various interference colors on the Al catalyst without dendrite structures, and Type 1 and Type 2 dendrite structures as evaluated by cross-polarized optical microscopy. The birefringent properties of grown GeS thin films are likely attenuated by thick Al as described in Figure 1j-l and Supporting Information Figure S1d-e, whereas they exhibit stronger interference colors on dendrite structures. Analogous birefringent properties have been noted elsewhere in an investigation of SnS flakes on a mica substrate [15]. Since this study is on the growth of GeS thin films, a thin film relaxation strategy [37, 38], namely annealing, is implemented to limit the formation of dendrite structures.

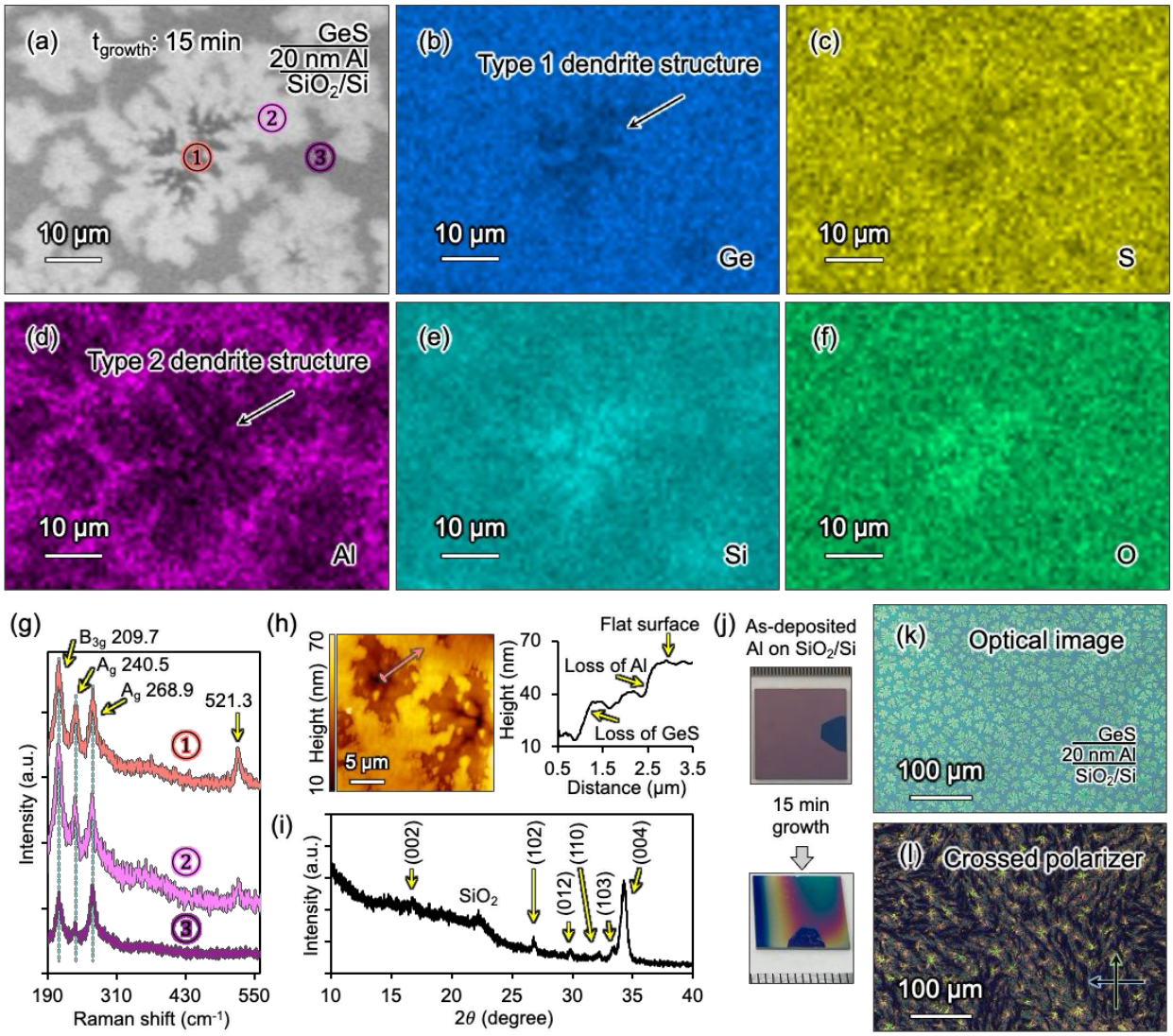

Figure 1. Evaluation of grown GeS thin films on SiO_2/Si substrate with 20 nm-thick Al deposited at room temperature. **(a)** Top view of SEM observation. **(b-f)** EDX mappings for Ge, S, Al, Si, and O, respectively. **(g)** Raman spectra of measured #1, #2 and #3 spots, respectively indicated in (a). **(h)** Surface morphology and depth profile of grown GeS thin films with 20 nm-thick Al. **(i)** XRD spectra of grown GeS thin films with the standard GeS reference of PDF#00-009-0231. **(j-l)** Photographs and microphotographs for 15-min growth of GeS using an optical microscope with and without a crossed polarizer.

If annealing is applied at 120 ˚C during 20 nm-thick Al deposition, the grown GeS thin film exhibits no dendrite structures, as demonstrated in Supporting Figure S2a and S2b. Annealing during Al deposition to reduce defects (internal stresses, atomic voids, etc.) as

evaluated here appears to be an effective method for growing GeS thin films. However, annealing during Al deposition under vacuum may result in hillock growth, agglomeration and other surface structures [39] with increasing film thickness, as seen in the SEM images of the thickness-dependent surface morphology of Al (Supporting Figures S2d-f). The thickness-dependent surface morphology of Al is analogous to the structure between Zone 1 and the Transition Zone [39], at deposition temperatures below $0.3T_{max}$ (T_{max} is the melting point of the deposited metal) as described by the extended structure zone model proposed by Thornton [65]. To prevent the formation of dendrite and surface structures in Al, we conducted a method using a 5 nm-thick Al deposited at room temperature. The as-deposited 5 nm-thick Al shows very few surface structure, as seen in the SEM image in Supporting Figure S2g. Time-dependent changes in the GeS growth process (3 and 5 min) with deposition at room temperature of 5 nm-thick Al on both SiO_2/Si and quartz substrates are shown in Figures 2a-h. Figures 2a and 2c are photographs of 3-min growth and Figures 2e and 2g show 5-min growth of GeS on SiO_2/Si and quartz substrates. Dendrite structure-free GeS thin films are obtained on SiO_2/Si and quartz substrates with a 5 nm-thick Al layer deposited at room temperature, analogous to that for a 20 nm-thick Al layer deposited and then annealed at 120 ˚C. Since no vapor-liquid-solid growth modes are observed, in the same way as seen with gold metal-catalyzed growth of GeS nanowires [7], the Al appears to stabilize the pre-deposited amorphous GeS layer and suppress the re-sublimation rate of the pre-deposited amorphous GeS layer.

Optical microscopy using a crossed polarizer is utilized to evaluate the birefringent properties of GeS thin films grown on SiO_2/Si and quartz substrates with growth times of 3 min (Figures 2b,2d) and 5 min (Figures 2f,2h), respectively. The darker regions, the so-called Maltese extinction cross pattern, are a common characteristic of radial anisotropic bodies between a crossed polarizer. The Maltese cross is parallel to the polarizer, and the analyzer orientations of the microscope are independent of the stage orientation. The Maltese cross results from the cancellation of birefringence every 90˚ with a crossed polarizer; for this reason, crystalline GeS along the vertical and horizontal directions is dark in the observed optical image. This suggests that the grown GeS thin film possesses a spherulite-like structure, since spherulite substances exhibit a Maltese cross pattern when observed using cross-polarized optical microscopy. The observed interference colors of spherulite-like GeS are likely affected by the thickness of the film and the underlying substrate, likely due to the birefringent properties of the

grown GeS thin film on the SiO_2/Si substrate. The thicker of the GeS film, the longer the reflected wavelength of the color observed, that is, moving it toward the red end of the spectrum. Conversely, the thinner the GeS film, the shorter the wavelength observed, moving it toward the blue end of the spectrum. In addition, if the polarizer is slightly rotated, GeS thin films show optically enhanced (blueish color) and weakened (reddish color) areas with different interference colors, as demonstrated in Supporting Figures S2h-k. It appears likely that the colored area shows the same structural orientation along the armchair or zigzag edge as sub-domains of crystallized GeS, present in the circular domain of spherulite-like GeS thin films. The formation of spherulite-like GeS thin films is likely attributable to a sharp local phase gradient in the adatom region of the growth front among the crystallized GeS, GeS vapor source and re-sublimated GeS from the Al catalyst [34, 66]. The ultrahigh supersaturation-induced condensation at the growth front likely results in the lateral growth of spherulite-like GeS at the interface of the sharp local phase gradient [57]. The diameter of one domain for spherulite-like GeS thin films with a 3-min growth time is about 450 - 500 μm, as shown in Figures 2b and 2d, whereas that for a 5-min growth time is about 700 μm, as shown in Figures 2f and 2h. The growth rate which achieves one circular domain with a diameter of hundreds of micrometers within 3 - 5 minutes, i.e., in the order of several micrometers per second (i.e., 2 - 3 μm/sec observed in this study), for the nonlinear spherulitic growth of GeS thin films, is analogous to the supercooling-like method.

Raman spectra of the grown spherulite-like GeS thin film on SiO_2/Si and quartz substrates are shown in Figure 2i, measured in four positions from the emanating center to the circular periphery and outside of the circular domain, as respectively denoted as the Centre, Middle, Fringe, and Remote areas. The Raman spectra noted at the emanated center (Centre), Middle and Fringe areas of the circular domain show three typical Raman phonon modes for GeS [63] as indicated by B_{3g} at 211 cm^{-1}, A_g at 240 cm^{-1} and A_g at 270 cm^{-1}, respectively representing the vibration mode of the zigzag edge direction, the layer breathing mode and the vibration mode of armchair edge direction. The Raman spectrum at 521 cm^{-1} corresponds to the Si substrate. Raman spectra of grown GeS thin films on quartz substrates are also obtained, whereas they generally show a downshift compared to that of on SiO_2/Si substrates. Raman spectra of grown GeS thin films on both SiO_2/Si and quartz substrates are not detected in the Remote area outside the circular domain. The lateral growth of GeS thin film is therefore attained by using the Al catalyst and pre-deposited amorphous GeS layers. Since AFM

measurements at the outside of the circular domains might affected by remaining pre-deposited amorphous GeS and Al, we employed cross-sectional SEM observations to evaluate thickness. These are described in the next paragraph. Therefore, only the surface roughness is shown in Figure 2j-k.

AFM measurements with a surface roughness R_a, of about 0.7 nm confirm the lateral growth of spherulite-like GeS thin films exhibiting a flat surface on both SiO_2/Si and quartz substrates. The fractal dendrite at the circular periphery is observed for grown GeS thin films on a quartz substrate as shown in the represented SEM image (Supporting Figure S2l). This likely confirms the Mullins-Sekerka instability at the growth front of the circular periphery [21–23], which is limited to only the normal growth mechanism for diffusion-limited growth; however, spherulite formation at the inner body of the grown GeS appears to be controlled by kinetic growth, since spherulites do not form under diffusion control. Diffusion-limited growth starts from the growth front at the periphery of the spherulite-like GeS after nucleation, following which there may be a transition region that facilitates a transformation from diffusion-limited growth [67] to kinetic-limited growth [68] for the body of spherulite-like GeS thin films. XRD spectra of the Al-catalyzed lateral growth of GeS thin films on both SiO_2/Si and quartz substrates are highlighted by green and yellow lines in Figure 2l. The XRD results confirm the orthorhombic lattice structure of GeS, in accordance with the standard GeS reference of PDF#00-009-0231. In the 2θ scan mode, the diffraction peaks that occur only at about 16.9˚ and 34.2˚ for (002) and (004) respectively are obtained, indicating that the crystal orientation is along the c-axis (001), and normal to the van der Waals stacking layers. This suggests that GeS thin films grown on SiO_2/Si and quartz substrates using 5 nm-thick Al and pre-deposited amorphous GeS consist of layered structures.

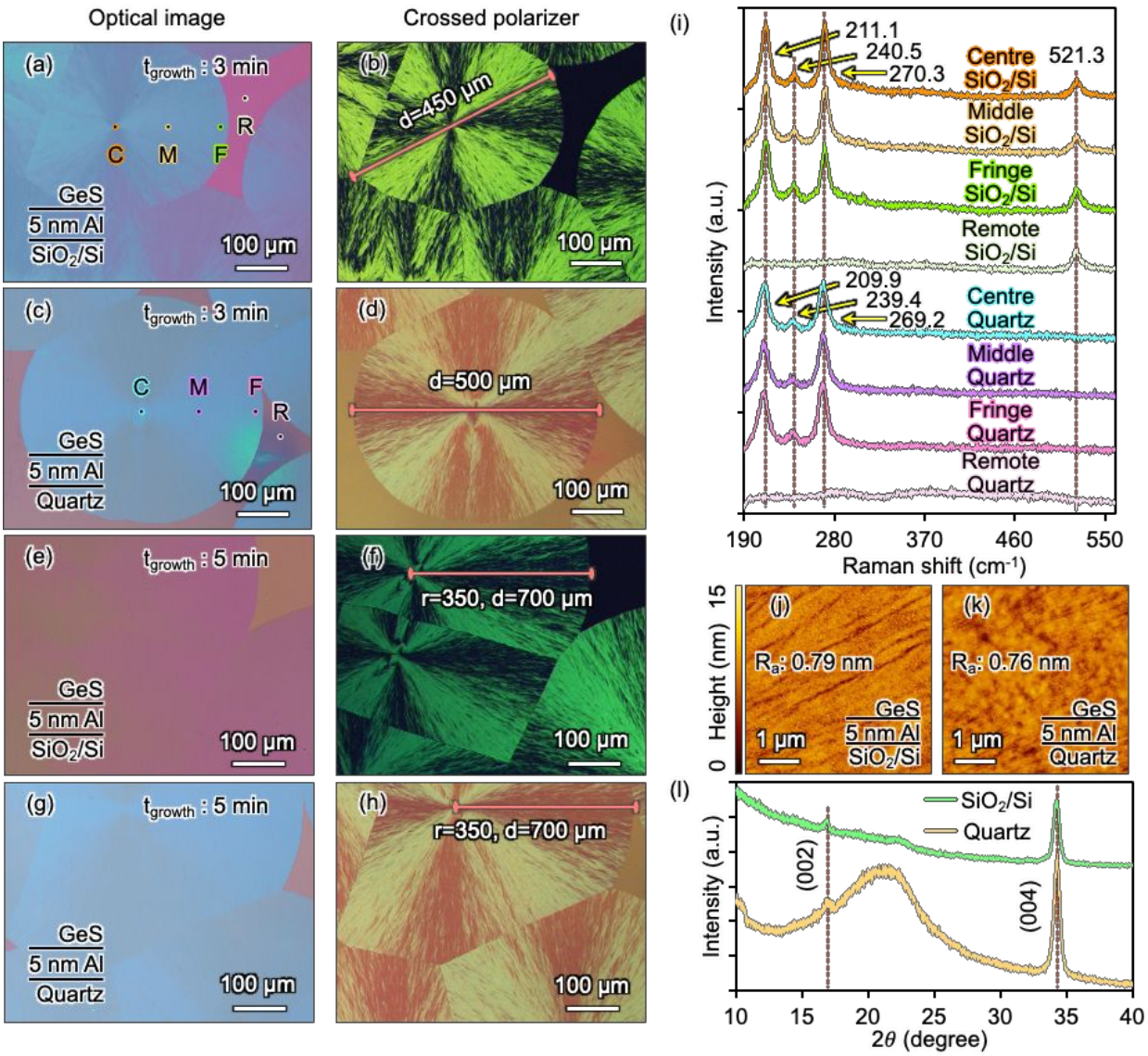

Figure 2. Evaluations of temporal change after 3 and 5 min for grown GeS thin films on SiO_2/Si and quartz substrates with 5 nm-thick Al deposited at room temperature. **(a-h)** Top view of optical microscope observations with and without applied crossed polarizer. r and d respectively represent the radius and diameter of one circular domain. **(i)** Raman spectra of measured spots at the Centre, Middle, Fringe and Remote spots on SiO_2/Si and quartz substrates as indicated in (a) and (c). **(j-k)** Surface morphology of grown GeS thin films with a 5 nm-thick Al on SiO_2/Si and quartz substrates, respectively. **(l)** XRD spectra of grown GeS thin films on insulating substrates with the standard GeS reference of PDF#00-009-0231.

Since a 15-min growth time is sufficient to fully cover the SiO_2/Si substrates with GeS, cross-sectional SEM measurements with EDX mappings were carried out to evaluate the thickness of the grown GeS thin films. The thickness of a grown GeS thin film is closely related to that of the pre-deposited amorphous GeS layer. To obtain various thicknesses of GeS thin films using a 5 nm-thick Al, a pressure control with identical flow of inlet Ar gas flux to achieve various thickness of pre-deposited amorphous GeS layer was applied. The observed various thicknesses of grown GeS thin films using a 5 nm-thick Al from areas highlighted by dashed circles are about 60 nm, 35 nm and 20 nm as shown in Figures 3a-c, attained by using pressures of 6500 Pa, 7000 Pa and 7500 Pa respectively during the pre-deposited amorphous GeS layer process. Insets of Figure 3a-c show overall photographs of Al-catalyzed grown GeS thin films on SiO_2/Si substrates. Cross-sectional EDX mappings for the elements Ge, S, Si and O in the grown approx. 60 nm-thick GeS thin film (as referenced in Figure 3a) are shown in Figure 3d-g. Ge and S are clearly obtained on top of the SiO_2/Si substrate. The two represented thicknesses measured using the provided software equipped with an SEM apparatus for the grown GeS thin film of about 35 nm and 20 nm are illustrated in Supporting Figure S3. The Al-catalyzed grown GeS thin films are much thinner than in our previous results (i.e., the observed minimum thickness of GeS is about 100 nm) [34], with a much lower variation in thickness of several tens of nanometers (in comparison with several micrometers in our previous results), facilitated by use of the optimized tilt susceptor method [40–42].

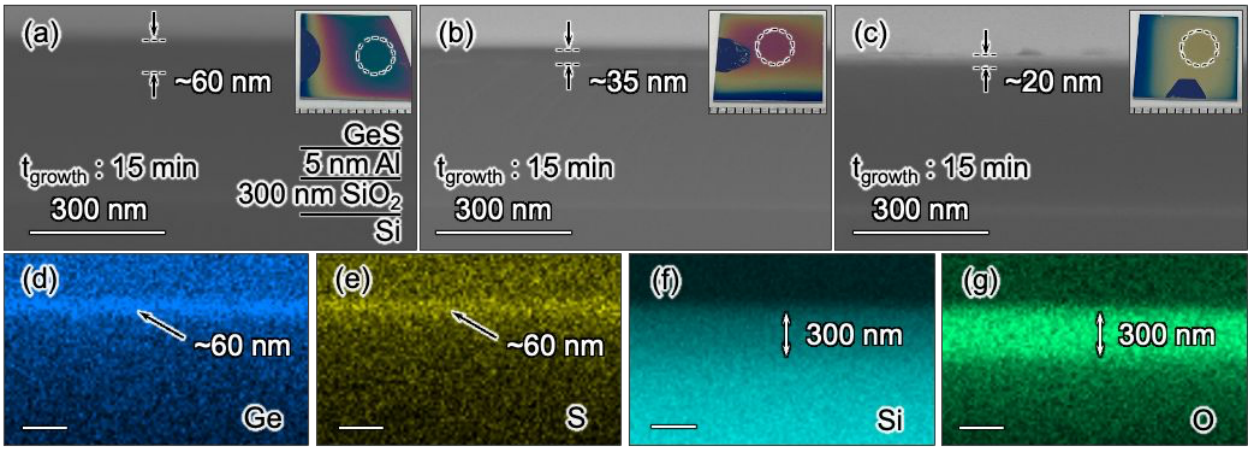

Figure 3. Cross-sectional SEM images for the thickness evaluation of 15-min growth of GeS thin films on SiO_2/Si substrates with 5 nm-thick Al deposited at room temperature. **(a-c)** Cross-sectional SEM observations with achieved thicknesses of 60 nm, 35 nm and 20 nm. Insets are photographs of the corresponding samples. **(d-g)** Cross-section EDX mappings for Ge, S, Si and O.

Since electron backscatter diffraction (EBSD) has been investigated to identify the cylindrically symmetric-rotating crystal InSiO [56] and the spherulite GeO_2 [57], it is considered to evaluate the crystallinity of grown spherulite-like GeS thin films and the Al deposited at elevated temperature in this study as well. However, it is extremely difficult to obtain any usable data using EBSD to identify the crystallinity or crystalline size of grown GeS thin films and the Al deposited at elevated temperatures. Observations of EBSD mappings, inverse pole figure (IPF) and IPF with 2 degrees intensity plot are shown in Supporting Figures S4a-h. Crystallinities of 5-nm and 20 nm-thick Al deposited at room-temperature and 120 ˚C on SiO_2/Si substrates exhibit amorphous-like states, analogous to that on bare SiO_2/Si substrates. Only the Al deposited on single-crystal Si (001) shows a single-crystal feature. In addition, crystallinities of about 60 nm-thick GeS thin films using 5-nm and 20 nm-thick Al on SiO_2/Si substrates show quite a number of areas in amorphous-like states, whereas the crystalline orientation of GeS (001) are slightly observed at certain areas. Observed amorphous-like crystallinities of Al-catalyzed grown GeS thin films are somewhat inconsistent with aforementioned XRD and Raman spectra, likely attributable to the amorphous GeS_x shell developed using the vapor transport method as investigated elsewhere [69]. It may simply be attributable to the uncertain factor that sulfur-containing compounds are not readily identifiable by the EBSD apparatus, as well. Thus, evaluation using transmission electron microscopy (TEM) is implemented for identifying the crystallinity of Al-catalyzed grown GeS thin films instead of further discussions regarding EBSD measurements of Al-catalyzed grown GeS thin films and deposited Al on SiO_2/Si substrates at elevated temperature in the current study.

Evaluation of the crystalline size of Al-catalyzed grown spherulite-like GeS thin films was investigated using TEM with selected-area electron diffraction (SAED) and EDX element mappings as shown in Figures 4a-h. As-grown 60 nm-thick GeS thin films with 5 nm-thick Al on 300-nm SiO_2/Si substrates were immersed in diluted hydrofluoric acid solutions to dissolve the

SiO_2 and metallic Al catalyst. The GeS thin films were then transferred to another beaker filled with deionized (DI) water. The delamination of GeS thin films from the as-grown SiO_2/Si substrate was observed immediately on the substrate being immersed in DI water, since the surface tension of the water is strong enough to separate the GeS from the substrate, which then floats on the surface of the DI water. An amorphous carbon-enhanced copper microgrid is then utilized to support the transferred GeS lamellae for TEM evaluations. High-resolution TEM (HRTEM) imaging shows the lattice fringe of the Al-catalyzed grown GeS, clearly exhibiting an orthorhombic structure [70] with zigzag- and armchair-edge directions as illustrated in Figure 4b. The fast Fourier transform pattern of the observed area in Figure 4b shows a clear, individual, and distinct diffraction pattern, confirming the crystallization of Al-catalyzed grown GeS in the limited observation area, as shown in the inset (Figure 4c). To identify the size of single-crystalline GeS, SAED with predetermined observation areas for aperture diameters of 200 nm to 16 μm was utilized. Observations of the crystalline size of the grown GeS as a function of these diameters are shown in Figure 3d-g. Typical GeS lamellae tend to adopt a clear single-crystalline structure of 200 nm in size with an individual and distinct diffraction pattern. Abnormal diffraction patterns, not associated with the orthorhombic atomic structure, are likely ascribable to the markedly different orientation of the GeS stitched at grain boundaries, or corrugated and overlapping structures resulting from the wet transfer process. On increasing the aperture to 800 nm in diameter, a slightly tiled and separated SAED pattern is observed, as shown in Figure 4e. At a diameter of 4 μm, the SAED pattern exhibits a slightly separated SAED pattern with a strong signal, although the amorphous diffraction ring is distinct (Figure 4f). The SAED pattern at a diameter of 16 μm shows discernible lathy diffraction patterns within the amorphous diffraction ring (Figure 4g). TEM, high-angle annular dark field scanning TEM (HADDF-STEM) and EDX element mappings are shown in Figure 4h. Aluminum shows a much lower signal than that of Ge and S, indicating that the Al should be removed so as to not affect the SAED patterns. Even though typical spherulite lamellae are radial with a small degree of divergence and observations of the Maltese extinction cross pattern under cross-polarized optical microscope are confirmed as mentioned in preceding sections [43–48, 50–57], it is not possible to state with full confidence that Al-catalyzed grown spherulite-like GeS thin films possess in-plane twisted structures as suggested solely by the observed lathy SAED patterns, without the confirmation of EBSD observations as investigated elsewhere [7, 46, 47, 56, 57]. Although the

rotating degree of diffraction patterns is relatively small and lathy, and the grown GeS thin films are confirmed by cross-polarized optical microscopy to possess a spherulite-like structure emanating from the circular domain center, it would be premature for us to conclude that the observed area of GeS lamellae indicates a pure polycrystalline structure. Further characterizations to identify the atomic lattice structures of grain boundaries and emanated centers in spherulite-like GeS thin films utilizing TEM and focused ion beam techniques will be needed in subsequent investigations. We therefore solely report a single-crystalline area of Al-catalyzed grown GeS thin film exceeding 200 nm in size.

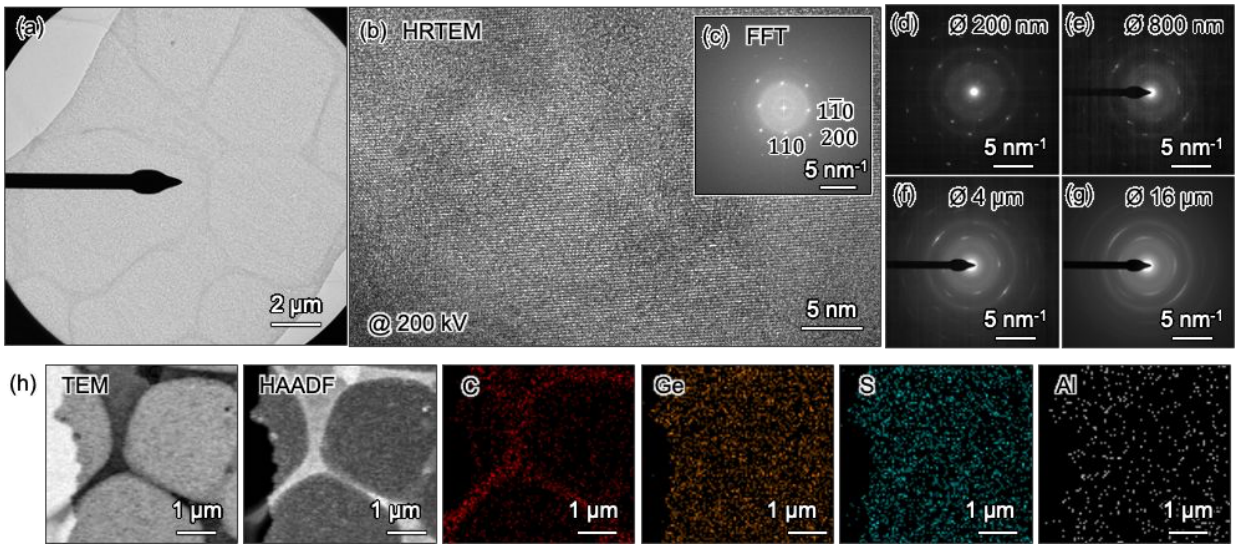

Figure 4. TEM evaluations of the crystallinity of GeS thin films grown for 15 min on SiO_2/Si substrates with a 5 nm-thick Al deposited at room temperature. **(a)** Top view of TEM observation supported by an amorphous carbon-enhanced copper microgrid after the wet transfer process. **(b-c)** High-resolution TEM image of a selected area, and its corresponding fast-Fourier transform (FFT) pattern. **(d-g)** SAED patterns of the observed area in (a) with aperture diameters of about 200 nm, 800 nm, 4 µm and 16 µm. **(h)** HADDF-STEM observations and corresponding EDX mappings of elemental C, Ge, S and Al.

3. CONCLUSIONS

In this study, germanium monosulfide (GeS) thin films with a minimum thickness of about 20 nm were laterally grown on SiO_2/Si (13 mm × 13 mm) and quartz (15 mm × 15 mm) substrates at a growth temperature of 420 ˚C, employing an Al catalyst synergistic with a pre-deposited amorphous GeS layer. Grown GeS thin films using a 20 nm-thick Al show dendrite structures. When annealing at 120 ˚C is applied during 20 nm-thick Al deposition, the grown GeS thin film exhibits no dendrite structures. Annealing the substrate during the thermal deposition of Al appears to be an effective method of reducing introduced defects caused by internal stress, atomic voids and so forth when growing GeS thin films. However, annealing during Al deposition under vacuum may result in hillock growth, agglomeration and other surface structures that result in increased film thickness, as predicted by Thornton's extended structure zone model. To prevent the formation of Al dendrite and surface structures, a method using a 5 nm-thick Al deposited at room temperature is implemented for the lateral growth of GeS thin films. The lateral growth rate of Al-catalyzed grown spherulite-like GeS thin films was observed to be 2 - 3 μm/sec.

The birefringent properties of Al-catalyzed grown GeS thin films with a Maltese extinction cross pattern were confirmed by using a cross-polarized optical microscope, indicating that the grown GeS has a spherulite-like structure. It is likely that the ultrahigh supersaturation-induced condensation due to Mullins-Sekerka instability takes place at the growth front at the edge of the circular domain, resulting in lateral growth of spherulite-like GeS thin films and showing a fractal or dendritic morphology. A transition region dominated by kinetic-limited diffusion likely occurs that creates the spherulite-like inner body of the GeS thin films, since spherulites do not form under diffusion control; and Mullins-Sekerka instability is limited to the normal growth mechanism of diffusion-limited growth. Moreover, the nonlinear spherulitic growth obtained in this study is analogous to the supercooling-like method. XRD spectra and AFM measurements show that the method applied in this study can result in the layered structure seen in spherulite-like GeS thin films with (002) and (004) crystal orientation and on flat surfaces on SiO_2/Si and quartz substrates. The observed TEM-SAED patterns suggest the crystals in the GeS to be larger than 200 nm. To summarize, this study proposes a potential method of growing lateral spherulite-like GeS thin films on insulating substrates (SiO_2/Si and quartz). It may also suggest that spherulite-like GeS holds the potential to achieve non-epitaxial single-crystalline functional semiconductors on insulating substrates, as previously investigated

for GeO_2 [57], for the development of next-generation GeS FETs (e.g., in-memory sensing and computing devices) with the potential advantage of creating programmable FETs via all-optical manipulation.

4. EXPERIMENTAL METHODS

GeS thin films are grown on insulating substrates such as 300 nm-SiO_2/Si and quartz using a horizontal quartz tube furnace with two independently-controlled heating regions. Approximately 20 mg GeS powder (99.99%, Sigma-Aldrich) is placed in a quartz boat in the upstream heating region. The SiO_2/Si (13 mm × 13 mm) and quartz (15 mm × 15 mm) substrates are cleaned by sonication in acetone for 15 min, then by repeated rinsing in isopropyl alcohol and deionized water. The substrates are then placed in the quartz tube in the downstream heating region with a tiled susceptor in a similar way to that used in our previous investigation [34]. The tube is evacuated to 0.015 Pa, followed by the supply of high-purity Ar carrier gas to reach the base pressure of 90 Pa by adjusting the needle valve in the gas feed-in line. Fluxed Ar gas for cleaning the growth environment of the quartz tube is maintained for at least 10 min. The growth temperature of the upstream heating region is increased to 440 ˚C, and that of the downstream heating region is increased to 420 ˚C 20 min later [34]. The three sets of pressures for the pre-deposited amorphous GeS layer are 6500, 7000, and 7500 Pa to grow GeS thin films about 60, 35, and 20 nm thick, respectively. The growth pressure is then maintained at around 6500 Pa by adjusting the vacuum valve in the exhaust line. The growth times are set to at 3, 5, and 15 min to evaluate the lateral growth and fully cover the substrates with GeS thin films. After growth, the quartz tube is cooled down rapidly to stop the growth process as soon as possible. Aluminum cut-wires (99.999% purity) are evaporated from an alumina-coated tungsten wire crucible and deposited on the SiO_2/Si and quartz substrates using a thermal evaporation apparatus with a heating stage. The deposition rate for various Al thicknesses is calibrated as 0.5 Å/sec using a quartz crystal sensor. 5 nm-thick Al is deposited at room temperature (RT) and 20 nm-thick Al is deposited at both RT and at the calibrated temperature of 120 ˚C.

Scanning electron microscopy (SEM) using a Hitachi SU8230 mounted with an energy-dispersive X-ray spectroscopy (EDX) detector were employed to investigate the defect structures

of grown GeS thin films. A Nikon Eclipse ME600 optical microscope with an angle-resolved polarizer was utilized to investigate the birefringent properties of the Al-catalyzed grown GeS thin films. The Raman microscopy observations were conducted at an excitation wavelength of 532 nm at a low laser power of about 20 μW to prevent any damage to the crystallized GeS. A PANalytical X'Pert PRO MRD X-ray diffractometer (XRD) with a Cu Kα source were utilized to collect XRD data in the range of 2θ from 10˚ to 40˚ in 0.01˚ steps. Transmission electron microscopy (TEM) operated at 200 kV with an EDX detector and selected area electron diffraction (SAED) in an FEI Talos F200X field emission microscope was utilized to investigate the crystallinity of the grown GeS thin films. The surface conditions were inspected using Hitachi atomic force probe equipment and an SII SPA 400. Electron backscatter diffraction (EBSD) measurements were conducted using a JEOL JSM-7900F with an EBSD detector.

ACKNOWLEDGMENTS

This work was supported by JSPS Kakenhi (Grants no. JP20K14796, JP23K13370 and JP24KF0164). Part of this work is also supported by the Advanced Research Infrastructure for Materials and Nanotechnology in Japan (ARIM), and MEXT Japan, proposal numbers 24NM5064 and 24UT1037. The author is grateful for helpful conversations with Prof. Dr. Nagashio of the University of Tokyo, and Drs. Tsukagoshi and Da of the National Institute for Materials Science, which brought birefringence and spherulite to the authors' attention.

AUTHOR INFORMATION

Corresponding Author

FUKATA.Naoki@nims.go.jp
ZHANG.Qinqiang@nims.go.jp

Present Addresses

† Research Center for Materials Nanoarchitectonics (MANA), National Institute for Materials Science (NIMS), Tsukuba, Ibaraki 305-0044, Japan

‡ Graduate School of Pure and Applied Sciences, University of Tsukuba, Tsukuba, Ibaraki 305-8573, Japan

Author contributions

The manuscript is written with contributions from all the authors. All the authors have approved the final version of the manuscript.

References

(1) Barraza-Lopez, S.; Fregoso, B. M.; Villanova, J. W.; Parkin, S. S. P.; Chang, K. Colloquium: Physical properties of group-IV monochalcogenide monolayers. *Reviews of Modern Physics* **2021**, *93* (1), 011001. DOI: 10.1103/RevModPhys.93.011001.

(2) Yu, M.; Hilse, M.; Zhang, Q.; Liu, Y.; Wang, Z.; Law, S. Review of Nanolayered Post-transition Metal Monochalcogenides Synthesis, Properties, and Applications. *ACS Applied Nano Materials* **2024**, *7* (24), 28008–28026. DOI: 10.1021/acsanm.3c05984.

(3) Li, C.; Huang, L.; Snigdha, G. P.; Yu, Y.; Cao, L. Role of Boundary Layer Diffusion in Vapor Deposition Growth of Chalcogenide Nanosheets The Case of GeS. *ACS Nano* **2012**, *6* (10), 8868-8877. DOI: 10.1021/nn303745e.

(4) Gomes, L. C.; Carvalho, A. Phosphorene analogues: Isoelectronic two-dimensional group-IV monochalcogenides with orthorhombic structure. *Physical Review B* **2015**, *92* (8), 085406. DOI: 10.1103/PhysRevB.92.085406.

(5) Wiley, J. D.; Breitschwerdt, A.; Schönherr, E. Optical absorption band edge in single-crystal GeS. *Solid State Communications* **1975**, *17* (3), 355-359. DOI: 10.1016/0038-1098(75)90311-7.

(6) Fei, R.; Kang, W.; Yang, L. Ferroelectricity and Phase Transitions in Monolayer Group-IV Monochalcogenides. *Phys Rev Lett* **2016**, *117* (9), 097601. DOI: 10.1103/PhysRevLett.117.097601.

(7) Sutter, P.; Wimer, S.; Sutter, E. Chiral twisted van der Waals nanowires. *Nature* **2019**, *570* (7761), 354-357. DOI: 10.1038/s41586-019-1147-x.

(8) Yan, Y.; Deng, Q.; Li, S.; Guo, T.; Li, X.; Jiang, Y.; Song, X.; Huang, W.; Yang, J.; Xia, C. In-plane ferroelectricity in few-layered GeS and its van der Waals ferroelectric diodes. *Nanoscale* **2021**, *13* (38), 16122-16130. DOI: 10.1039/d1nr03807a.

(9) Luo, D.; Zhang, B.; Sie, E. J.; Nyby, C. M.; Fan, Q.; Shen, X.; Reid, A. H.; Hoffmann, M. C.; Weathersby, S.; Wen, J.; et al. Ultrafast Optomechanical Strain in Layered GeS. *Nano Lett* **2023**, *23* (6), 2287-2294. DOI: 10.1021/acs.nanolett.2c05048.

(10) Sutter, E.; Komsa, H.-P.; French, J. S.; Sutter, P. Composition Dependence of the Band Gaps of Semiconducting GeSxSe1–x van der Waals Alloys. *Chemistry of Materials* **2023**, *35* (16), 6374-6381. DOI: 10.1021/acs.chemmater.3c01069.

(11) Liu, Y.; Wang, J.; Kim, S.; Sun, H.; Yang, F.; Fang, Z.; Tamura, N.; Zhang, R.; Song, X.; Wen, J.; et al. Helical van der Waals crystals with discretized Eshelby twist. *Nature* **2019**, *570* (7761), 358-362. DOI: 10.1038/s41586-019-1308-y.

(12) Sutter, E.; Wang, J.; Sutter, P. Lateral Heterostructures of Multilayer GeS and SnS van der Waals Crystals. *ACS Nano* **2020**, *14* (9), 12248-12255. DOI: 10.1021/acsnano.0c05978.

(13) Jia, S.; Li, H.; Gotoh, T.; Longeaud, C.; Zhang, B.; Lyu, J.; Lv, S.; Zhu, M.; Song, Z.; Liu, Q.; et al. Ultrahigh drive current and large selectivity in GeS selector. *Nature Communications* **2020**, *11* (1), 4636. DOI: 10.1038/s41467-020-18382-z.

(14) Sutter, E.; Ghimire, P.; Sutter, P. Directing Charge Carriers and Ferroelectric Domains at Lateral Interfaces in van der Waals Heterostructures. *ACS Nano* **2024**, *18* (44), 30829-30837. DOI: 10.1021/acsnano.4c11341.

(15) Nanae, R.; Kitamura, S.; Chang, Y. R.; Kanahashi, K.; Nishimura, T.; Moqbel, R.; Lin, K. H.; Maruyama, M.; Gao, Y.; Okada, S.; et al. Bulk Photovoltaic Effect in Single Ferroelectric Domain of SnS Crystal and Control of Local Polarization by Strain. *Advanced Functional Materials* **2024**, *34* (41), 2406140. DOI: 10.1002/adfm.202406140.

(16) Sutter, E.; Ghimire, P.; Sutter, P. Macroscopic Monochalcogenide van der Waals Ferroics: Growth, Domain Structures, and Curie Temperature. *J Am Chem Soc* **2024**, *146* (46), 31961-31968. DOI: 10.1021/jacs.4c11558.
(17) Xin, C.; Zheng, J.; Su, Y.; Li, S.; Zhang, B.; Feng, Y.; Pan, F. Few-Layer Tin Sulfide: A New Black-Phosphorus-Analogue 2D Material with a Sizeable Band Gap, Odd–Even Quantum Confinement Effect, and High Carrier Mobility. *The Journal of Physical Chemistry C* **2016**, *120* (39), 22663-22669. DOI: 10.1021/acs.jpcc.6b06673.
(18) Bao, Y.; Song, P.; Liu, Y.; Chen, Z.; Zhu, M.; Abdelwahab, I.; Su, J.; Fu, W.; Chi, X.; Yu, W.; et al. Gate-Tunable In-Plane Ferroelectricity in Few-Layer SnS. *Nano Lett* **2019**, *19* (8), 5109-5117. DOI: 10.1021/acs.nanolett.9b01419.
(19) Shan, Y.; Li, Y.; Pang, H. Applications of Tin Sulfide‐Based Materials in Lithium‐Ion Batteries and Sodium‐Ion Batteries. *Advanced Functional Materials* **2020**, *30* (23), 2001298. DOI: 10.1002/adfm.202001298.
(20) Chang, K.; Parkin, S. S. P. Experimental formation of monolayer group-IV monochalcogenides. *Journal of Applied Physics* **2020**, *127* (22), 220902. DOI: 10.1063/5.0012300.
(21) Mullins, W. W.; Sekerka, R. F. Morphological Stability of a Particle Growing by Diffusion or Heat Flow. *Journal of Applied Physics* **1963**, *34* (2), 323-329. DOI: 10.1063/1.1702607.
(22) Mullins, W. W.; Sekerka, R. F. Stability of a Planar Interface During Solidification of a Dilute Binary Alloy. *Journal of Applied Physics* **1964**, *35* (2), 444-451. DOI: 10.1063/1.1713333.
(23) Sekerka, R. F. A Stability Function for Explicit Evaluation of the Mullins-Sekerka Interface Stability Criterion. *Journal of Applied Physics* **1965**, *36* (1), 264-268. DOI: 10.1063/1.1713887.
(24) Feng, M.; Liu, S. C.; Hu, L.; Wu, J.; Liu, X.; Xue, D. J.; Hu, J. S.; Wan, L. J. Interfacial Strain Engineering in Wide-Bandgap GeS Thin Films for Photovoltaics. *Journal of the American Chemical Society* **2021**, *143* (25), 9664-9671. DOI: 10.1021/jacs.1c04734.
(25) Mao, Y.; Chen, N.; Deng, T.; Lan, Z. Two-dimensional GeS synthesized by one-step space-confined APCVD and its self-powered photodetector. *Physica B: Condensed Matter* **2024**, *685*, 415984. DOI: 10.1016/j.physb.2024.415984.
(26) Drabavičius, A.; Pakštas, V.; Jasiūnas, R.; Koltsov, M.; Talaikis, M.; Naujokaitis, A.; Spalatu, N.; Kondrotas, R.; Gulbinas, V.; Franckevičius, M. Synthesis and characterization of polycrystalline GeS thin films for optoelectronic applications. *Materials Science in Semiconductor Processing* **2025**, *188*. DOI: 10.1016/j.mssp.2024.109193.
(27) Li, X.; Cai, W.; An, J.; Kim, S.; Nah, J.; Yang, D.; Piner, R.; Velamakanni, A.; Jung, I.; Tutuc, E.; et al. Large-Area Synthesis of High-Quality and Uniform Graphene Films on Copper Foils. *Science* **2009**, *324* (5932), 1312-1314. DOI: 10.1126/science.1171245.
(28) Xu, X.; Zhang, Z.; Qiu, L.; Zhuang, J.; Zhang, L.; Wang, H.; Liao, C.; Song, H.; Qiao, R.; Gao, P.; et al. Ultrafast growth of single-crystal graphene assisted by a continuous oxygen supply. *Nat Nanotechnol* **2016**, *11* (11), 930-935. DOI: 10.1038/nnano.2016.132.
(29) Liu, K. K.; Zhang, W.; Lee, Y. H.; Lin, Y. C.; Chang, M. T.; Su, C. Y.; Chang, C. S.; Li, H.; Shi, Y.; Zhang, H.; et al. Growth of large-area and highly crystalline MoS2 thin layers on insulating substrates. *Nano Lett* **2012**, *12* (3), 1538-1544. DOI: 10.1021/nl2043612.
(30) Li, S.; Lin, Y. C.; Zhao, W.; Wu, J.; Wang, Z.; Hu, Z.; Shen, Y.; Tang, D. M.; Wang, J.; Zhang, Q.; et al. Vapour-liquid-solid growth of monolayer MoS(2) nanoribbons. *Nat Mater* **2018**, *17* (6), 535-542. DOI: 10.1038/s41563-018-0055-z.

(31) Li, S.; Lin, Y.-C.; Hong, J.; Gao, B.; Lim, H. E.; Yang, X.; Liu, S.; Tateyama, Y.; Tsukagoshi, K.; Sakuma, Y.; et al. Mixed-Salt Enhanced Chemical Vapor Deposition of Two-Dimensional Transition Metal Dichalcogenides. *Chemistry of Materials* **2021**, *33* (18), 7301-7308. DOI: 10.1021/acs.chemmater.1c01652.
(32) Kodambaka, S.; Tersoff, J.; Reuter, M. C.; Ross, F. M. Germanium Nanowire Growth Below the Eutectic Temperature. *Science* **2007**, *316* (5825), 729-732. DOI: 10.1126/science.1139105.
(33) Clark, J. B.; Pistorius, C. W. F. T. The aluminium-germanium eutectic temperature to 40 kilobars. *Journal of the Less-Common Metals* **1974**, *34* (2), 233-236. DOI: 10.1016/0022-5088(74)90164-7.
(34) Zhang, Q.; Matsumura, R.; Fukata, N. Synthesis of Large-Area GeS Thin Films with the Assistance of Pre-deposited Amorphous Nanostructured GeS Films: Implications for Electronic and Optoelectronic Applications. *ACS Applied Nano Materials* **2023**, *6* (8), 6920-6928. DOI: 10.1021/acsanm.3c00669.
(35) Semaltianos, N. G. Thermally evaporated aluminium thin films. *Applied Surface Science* **2001**, *183* (3-4), 223-229. DOI: 10.1016/S0169-4332(01)00565-7.
(36) Blakeney, K. J.; Winter, C. H. Atomic Layer Deposition of Aluminum Metal Films Using a Thermally Stable Aluminum Hydride Reducing Agent. *Chemistry of Materials* **2018**, *30* (6), 1844-1848. DOI: 10.1021/acs.chemmater.8b00445.
(37) Lahiri, S. K. Stress Relief and Hillock Formation in Thin Lead Films. *Journal of Applied Physics* **1970**, *41* (7), 3172-3176. DOI: 10.1063/1.1659383.
(38) Abermann, R. Internal stress of vapour-deposited aluminium films Effect of O2 and water vapour present during film deposition. *Thin Solid Films* **1990**, *186* (2), 233-240. DOI: 10.1016/0040-6090(90)90145-4.
(39) Thornton, J. A. HIGH RATE THICK FILM GROWTH. *Annual review of materials science,* **1977**, *7* (1), 239-260.
(40) Amano, H.; Sawaki, N.; Akasaki, I.; Toyoda, Y. Metalorganic vapor phase epitaxial growth of a high quality GaN film using an AlN buffer layer. *Applied Physics Letters* **1986**, *48* (5), 353-355. DOI: 10.1063/1.96549.
(41) Pierson, H. O.; Lieberman, M. L. The chemical vapor deposition of carbon on carbon fibers. *Carbon* **1975**, *13* (3), 159-166. DOI: 10.1016/0008-6223(75)90226-2.
(42) Choy, K. L. Chemical vapour deposition of coatings. *Progress in Materials Science* **2003**, *48* (2), 57-170. DOI: 10.1016/S0079-6425(01)00009-3.
(43) Keith, H. D.; Padden, F. J. Spherulitic Crystallization from the Melt. I. Fractionation and Impurity Segregation and Their Influence on Crystalline Morphology. *Journal of Applied Physics* **1964**, *35* (4), 1270-1285. DOI: 10.1063/1.1713606.
(44) Shtukenberg, A. G.; Punin, Y. O.; Gunn, E.; Kahr, B. Spherulites. *Chem Rev* **2012**, *112* (3), 1805-1838. DOI: 10.1021/cr200297f.
(45) Hosier, I. L.; Bassett, D. C. A study of the morphologies and growth kinetics of three monodisperse n-alkanes C122H246, C162H326 and C246H494. *Polymer* **2000**, *41* (25), 8801-8812. DOI: 10.1016/S0032-3861(00)00223-8.
(46) Oaki, Y.; Imai, H. Amplification of Chirality from Molecules into Morphology of Crystals through Molecular Recognition. *Journal of the American Chemical Society* **2004**, *126* (30), 9271-9275. DOI: 10.1021/ja048661.
(47) Imai, H.; Oaki, Y. Emergence of morphological chirality from twinned crystals. *Angew Chem Int Ed Engl* **2004**, *43* (11), 1363-1368. DOI: 10.1002/anie.200352891.

(48) Geveling, N. N.; Maslenkov, S. B. Solidification of eutectic Ni-Ni3Ti alloys. *Metal Science and Heat Treatment* **1976**, *18*, 755-760. DOI: 10.1007/BF00704110.
(49) Matsumura, R.; Sasaki, M.; Chikita, H.; Sadoh, T.; Miyao, M. Thickness Dependent Solid-Phase Crystallization of Amorphous GeSn on Insulating Substrates at Low Temperatures (<=250 C). *ECS Solid State Letters* **2015**, *4* (12), P95-P97. DOI: 10.1149/2.0021512ssl.
(50) Jin, L.-W.; Claborn, K. A.; Kurimoto, M.; Geday, M. A.; Maezawa, I.; Sohraby, F.; Estrada, M.; Kaminksy, W.; Kahr, B. Imaging linear birefringence and dichroism in cerebral amyloid pathologies. *Proceedings of the National Academy of Sciences* **2003**, *100* (26), 15294-15298. DOI: 10.1073 pnas.2534647100.
(51) Al-Atar, U.; Bokov, A. A.; Marshall, D.; Teichman, J. M. H.; Gates, B. D.; Ye, Z.-G.; Branda, N. R. Mechanism of Calcium Oxalate Monohydrate Kidney Stones Formation: Layered Spherulitic Growth. *Chemistry of Materials* **2010**, *22* (4), 1318-1329. DOI: 10.1021/cm901751g.
(52) Granasy, L.; Pusztai, T.; Tegze, G.; Warren, J. A.; Douglas, J. F. Growth and form of spherulites. *Phys Rev E Stat Nonlin Soft Matter Phys* **2005**, *72* (1), 011605. DOI: 10.1103/PhysRevE.72.011605.
(53) Tanaka, H.; Nishi, T. Local phase separation at the growth front of a polymer spherulite during crystallization and nonlinear spherulitic growth in a polymer mixture with a phase diagram. *Phys Rev A Gen Phys* **1989**, *39* (2), 783-794. DOI: 10.1103/physreva.39.783.
(54) Shtukenberg, A. G.; Tan, M.; Vogt-Maranto, L.; Chan, E. J.; Xu, W.; Yang, J.; Tuckerman, M. E.; Hu, C. T.; Kahr, B. Melt Crystallization for Paracetamol Polymorphism. *Crystal Growth & Design* **2019**, *19* (7), 4070-4080. DOI: 10.1021/acs.cgd.9b00473.
(55) Okada, T.; Saito, H.; Inoue, T. Nonlinear crystal growth in the mixture of isotactic polypropylene and liquid paraffin. *Macromolecules* **1990**, *23* (16), 3865-3868. DOI: 10.1021/ma00218a024.
(56) Da, B.; Cheng, L.; Liu, X.; Shigeto, K.; Zhang, Z.; Tsukagoshi, K.; Nabatame, T.; Ding, Z.; Liu, J.; Yoshikawa, H.; et al. Exploring high-symmetry structures in non-Cartesian coordinates: preparation and characteristics of cylindrically symmetric-rotating crystals. *Science and Technology of Advanced Materials: Methods* **2024**, *4* (1), 2406743. DOI: 10.1080/27660400.2024.2406743.
(57) Zhou, S.; Antoja-Lleonart, J.; Nukala, P.; Ocelík, V.; Lutjes, N. R.; Noheda, B. Crystallization of GeO2 thin films into α-quartz: from spherulites to single crystals. *Acta Materialia* **2021**, *215*, 117069. DOI: 10.1016/j.actamat.2021.117069.
(58) Kim, H.; Lee, S.; Shin, J.; Zhu, M.; Akl, M.; Lu, K.; Han, N. M.; Baek, Y.; Chang, C. S.; Suh, J. M.; et al. Graphene nanopattern as a universal epitaxy platform for single-crystal membrane production and defect reduction. *Nat Nanotechnol* **2022**, *17* (10), 1054-1059. DOI: 10.1038/s41565-022-01200-6.
(59) Kim, K. S.; Lee, D.; Chang, C. S.; Seo, S.; Hu, Y.; Cha, S.; Kim, H.; Shin, J.; Lee, J. H.; Lee, S.; et al. Non-epitaxial single-crystal 2D material growth by geometric confinement. *Nature* **2023**, *614* (7946), 88-94. DOI: 10.1038/s41586-022-05524-0.
(60) Ghosh, S.; Zheng, Y.; Zhang, Z.; Sun, Y.; Schranghamer, T. F.; Sakib, N. U.; Oberoi, A.; Chen, C.; Redwing, J. M.; Yang, Y.; et al. Monolithic and heterogeneous three-dimensional integration of two-dimensional materials with high-density vias. *Nature Electronics* **2024**, *7* (10), 892-903. DOI: 10.1038/s41928-024-01251-8.
(61) Kang, J. H.; Shin, H.; Kim, K. S.; Song, M. K.; Lee, D.; Meng, Y.; Choi, C.; Suh, J. M.; Kim, B. J.; Kim, H.; et al. Monolithic 3D integration of 2D materials-based electronics

towards ultimate edge computing solutions. *Nat Mater* **2023**, *22* (12), 1470-1477. DOI: 10.1038/s41563-023-01704-z.

(62) Chen, C.; Yi, Z. Photostrictive Effect: Characterization Techniques, Materials, and Applications. *Advanced Functional Materials* **2021**, *31* (22), 2010706. DOI: 10.1002/adfm.202010706.

(63) Chandrasekhar, H. R.; Humphreys, R. G.; Cardona, M. Pressure dependence of the Raman spectra of the IV-VI layer compounds GeS and GeSe. *Physical Review B* **1977**, *16* (6), 2981-2983. DOI: 10.1103/PhysRevB.16.2981.

(64) Gu, J.; Shi, Y.; Du, Z.; Li, M.; Yang, S. Stress Relief in Metal Anodes: Mechanisms and Applications. *Advanced Energy Materials* **2023**, *13* (40), 2302091. DOI: 10.1002/aenm.202302091.

(65) Thornton, J. A. Influence of substrate temperature and deposition rate on structure of thick sputtered Cu coatings. *Journal of Vacuum Science and Technology* **1975**, *12* (4), 830-835. DOI: 10.1116/1.568682.

(66) Kaye, G. W. C.; Ewen, D. The sublimation of Metals at Low pressures. *Proceedings of the Royal Society of London. Series A, Containing Papers of a Mathematical and Physical Character* **1913**, *89* (607), 58-67. DOI: 10.1098/rspa.1913.0063.

(67) Seki, K.; Saiki, K. Transition from Reaction- to Diffusion-Limited Growth of Graphene by Chemical Vapor Deposition. *Crystal Growth & Design* **2022**, *22* (7), 4396-4403. DOI: 10.1021/acs.cgd.2c00363.

(68) Sobolev, S. L. On the transition from diffusion-limited to kinetic-limited regimes of alloy solidification. *Acta Materialia* **2013**, *61* (20), 7881-7888. DOI: 10.1016/j.actamat.2013.09.027.

(69) Sutter, E.; Zhang, B.; Sun, M.; Sutter, P. Few-Layer to Multilayer Germanium(II) Sulfide: Synthesis, Structure, Stability, and Optoelectronics. *ACS Nano* **2019**, *13* (8), 9352-9362. DOI: 10.1021/acsnano.9b03986.

(70) Wiedemeier, H.; Schnering, H. G. v. Refinement of the structures of GeS, GeSe, SnS and SnSe. *Zeitschrift für Kristallographie - Crystalline Materials* **1978**, *148* (3-4), 295-303. DOI: 10.1524/zkri-1978-3-410.